Materials Today Communications 35 (2023) 106010

Contents lists available at ScienceDirect

Materials Today Communications

journal homepage: www.elsevier.com/locate/mtcomm

Influence of material anisotropy on void coalescence by necking for face-centered cubic single crystals

Gopi Gulivindala [a], Madhu Kiran Karanam [a], Kwong Ming Tse [b], Viswanath Chinthapenta [a,*]

[a] Micromechanics Lab, Department of Mechanical and Aerospace Engineering, Indian Institute of Technology Hyderabad, Telangana, 502284, India
[b] Department of Mechanical and Product Design Engineering, School of Engineering, Swinburne University of Technology, Australia

ARTICLE INFO

Keywords:
Ductile fracture
Void coalescence
Multi-point constraints
Load path parameters
Material anisotropy

ABSTRACT

This paper presents the coalescence of microvoids embedded in an anisotropic copper single crystal using a micromechanics approach. Crystal plasticity framework was used to account for the anisotropy arising from the orientation and slip. A full 3D representative volume element (RVE) with void was considered to circumvent spurious loading. The constant load path parameters were enforced on the RVE using multi-point constraints. Various loading conditions that lead to necking were studied. The key finding from the present study is the interplay of the load path parameters (triaxiality and Lode parameter), material anisotropy, and initial void volume fraction on the void coalescence. It is noticed that at high triaxiality, the ductile failure mechanism is dominated by the necking mechanism, and at medium to low triaxiality, the ductile failure mode is a combination of shearing and necking mechanisms. It was observed that non-homogenous crystallographic slip manifests the material anisotropic effects in void cell RVE across various crystallographic orientations. The crystal orientation [110] exhibited higher shearing than the orientation [100] and [111]. Further, material anisotropy significantly affected void morphology but not the void coalescence strains at high triaxial values.

1. Introduction

The mechanistic approach for ductile failure assessment of structural components enables the development of efficient predictive failure models [1]. Ductile failure in metals and their alloys can occur without or with voids. Necking down to a point and catastrophic shear along the single plane [2] or multiple planes [3] are ductile fracture mechanisms without voids. In the other case, microvoids form due to fracture or decohesion of secondary phase particles from the matrix [4]. The microvoids grow under the multiaxial tensile loading and fail without [5] or with coalescence [6]. In Orowan alternating slip failure, the microvoid initiates at the juncture of two shear bands, grows prismatically, and fails without coalescence [5]. This study focuses on the ductile failure that occurs through void coalescence, which is one of the most important ductile fracture mechanisms [6].

Over the last five decades, several researchers have investigated ductile fracture using experiments [7–12] and phenomenological [13–22] models. Bluhm and Morrissey [7] performed ductile fracture experiments on a round Copper (Cu) bar under tensile loading. They detected the void nucleation using an ultrasonic technique and showed that the onset of void coalescence could be identified by a sudden knee on the load-deflection curve. Void nucleation generally occurs either at grain boundaries [8] or within the grain under different conditions. The nucleation of voids at the grain boundaries is often associated with the presence of inclusions [4,8,12]. On the other hand, void nucleation within the grain occurs in pure metals with no inclusions. The study by Noell et al. [9] on Cu demonstrated that it is possible to have voids nucleate inside the grain without inclusions because of vacancy condensation. Even in a polycrystalline Cu, when the voids originate at inclusion and are embedded in coarse grain [23], the void size is minimal compared to the grain size. The voids in such a scenario develop as if they are embedded in a single crystal.

Studying ductile failure in a single crystal has an added advantage in its well-established slip system. Therefore, investigation of the ductile failure of Cu single crystals can provide valuable insights into the development of ductile damage models [24]. Ward et al. [8] showed the presence of many small diameter ($\sim$1 μm) microvoids and a few large diameter ($\sim$100 μm) microvoids in the failure section using fractographic studies on Oxygen Free High Conductivity (OFHC) copper. They observed that the smaller voids were mostly benign in nature. Puttick [4] showed that the large microvoids enlarge until strain hardening of the material exhausts. The material softens because of the increase in

* Corresponding author.
E-mail address: viswanath@mae.iith.ac.in (V. Chinthapenta).

https://doi.org/10.1016/j.mtcomm.2023.106010
Received 10 February 2023; Received in revised form 5 April 2023; Accepted 13 April 2023
Available online 14 April 2023

void volume fraction (f) [7]. The enlarged voids coalesce by thinning down the ligament length (LL) between the voids [10,11]. The fractured surfaces investigation showed that it has dimple structured or smooth shear surfaces, indicating a ductile failure [11].

Meanwhile, Gurson [13] developed an analytical yield locus for void cells based on the upper bound approach for cylindrical and spherical voids in a fully plastic flow matrix and an empirical locus for a matrix with a rigid section. Rice and Tracey [14] showed an exponential increase in f (void growth) under high-stress triaxiality (T). While Huang [15] reworked the Rice and Tracey model and proposed two models for void growth, one for low values of T and the other for high values of T. The void growth approximation by Rice and Tracey underestimates by 50 % for the values of $T > 1$. Pardoen and Hutchison [16] used one tuning parameter (q) and avoided the usage of the (phenomenological parameter) void volume fraction at the onset of coalescence (f_c) to develop a micromechanics-based void growth model. The models by Rice and Tracey [14] and Huang [15] are based on rigid-plastic void cells, whereas Pardoen and Hutchison's [16] model used axisymmetric elastoplastic void cells. Pardoen and Hutchison's model provides better prediction over an extensive range of porosity, void shape, cell aspect ratio, triaxiality, and matrix flow behavior. The evolution of f has contributions from the void growth of preexisted voids as well as the nucleation of secondary voids [17]. Chu and Needleman [18] proposed an approximate function to determine the contribution to f from void nucleation based on the normal distribution. It relates the void volume fraction of the secondary phase particles and inclusions, plastic strain, and nucleation strain.

Gurson's yield function included a simplified representation of damage and its evolution based on the initial void volume fraction (f_0). It considers the shape of void to remain the same, i.e., spherical voids remain spherical and cylindrical voids remain cylindrical. Further, it was modified by Tvergaard [19] as Gurson-Tvergaard (GT) model by incorporating three calibration parameters (q_1, q_2, q_3) to include the effect of void shape. The GT model is reasonably applicable until the void evolution is below f_c. Tvergaard and Needleman [25] extended the GT model by accounting for final material failure after the onset of void coalescence through an inequality bifurcating the f before and after f_c. The Gurson-Tvergaard-Needleman (GTN) model has been extensively adopted in the literature and provides the fundamental framework for damage-based modeling [26–28]. The GLD (Gologanu-Leblond-Devaux) model was developed by Gologanu et al. [20] by including the void shape effects in the Gurson model. Ragab [21] compiled analytical and finite element results on yield function models and developed a semi-empirical equation suitable for an extensive range of void shapes, materials, and triaxialities, with limitations on void shape. There are few studies on finding the void coalescence analytically; for example, Keralaverma and Chockalingam [22] incorporated material anisotropic effects in Hill orthotropic rigid ideal plastic material and found closed form criterion for coalescence of cylindrical voids. The phenomenological parameters in the above-mentioned analytical approaches [13–22] can be identified using micromechanics-based simulations. Other than crystalline materials, the anisotropic and nonlinear effects influence the material properties in several other classes of materials [29–31].

Numerical investigations on the representative volume element (RVE) were performed in the literature to overcome the difficult experiments and to estimate the onset of void coalescence [32]. Koplik and Needleman's [33] numerical work on elastic viscoplastic isotropic hardening material with a periodical array of spherical voids showed a shift in deformation from an axisymmetric state to uniaxial straining at the onset of void coalescence. Kim et al. [1] studied the effect of stress triaxiality (T) and initial porosity (f_0) on void growth and coalescence using simple axisymmetric RVE with a spherical void embedded at the center. The phenomenological constitutive models with a finite-element-based framework in the above literature have several limitations, such as being restricted to isotropic materials. Advanced simulation techniques such as mechanistic-based crystal plasticity simulations [34–36] and molecular dynamics (MD) simulations [37–39] can overcome the limitations posed by the phenomenological frameworks. MD simulations can capture the anisotropy and discreteness in modeling the porous nanomaterials, phase transformations, and temperature effects. While crystal plasticity can capture the crystallographic slip and anisotropy efficiently.

The present work used the 3D crystal plasticity framework to understand the role of void volume fraction and crystallographic-slip-driven shear deformation on void coalescence. Yerra et al. [35] estimation of void coalescence was within 20 % of Thomason's coalescence criteria. They observed that void evolution is strongly dependent on T [1,33,34]. However, at low T, Barsoum and Faleskog [10] showed that the T alone could not uniquely represent the triaxial loading [1,11]. They observed that the Lode parameter (L) significantly affects coalescence at low values of T. Guo and Wong [40] also found that the difference between the void coalescence strains for different L values is decreasing with increasing triaxiality. While Vishwakarma and Keralavarma's multi-surface plasticity model predicts the onset of void coalescence strain and its dependence on T and L. Their model predicts better for medium to high T only. Chouksey and Keralavarma's [41] study revealed that void coalescence strains based on the critical damage variable are inconsistent, as they are phenomenological in nature. A recent study by Guo et al. [42] estimated the void coalescence strain (E_{eqc}) under multiaxial loading using 3D crystal plasticity simulations and proposed a relation for estimating the onset of void coalescence strain as a function of the novel equivalent loading parameter. They observed that L strongly influences the onset of void coalescence strains at low values of T.

The void coalescence mechanism depends on parameters like void geometry (f_0, shape), void spacing, load path parameters (T and L), and material hardening [37]. The three types of void coalescences failure mechanisms: (a) necking, (b) shearing of inter void ligament, and (c) void impingement, strongly depend on the multiaxial loading conditions. The void grows and coalesces in the axial direction in the case of necking, as shown in Fig. 1(a). Failure by the necking mechanism occurs only at high-stress triaxialities [35]. Void coalescence occurs in 45^0 to the axial direction for the case of shearing, as shown in Fig. 1(b), usually observed at low-stress triaxialities [35]. Barsoum and Faleskog [10,11] found that, generally, the failure is a combination of shearing and necking mechanisms that occurs at the low to medium stress triaxiality. Whereas in the case of void impingement, two voids grow and come into contact, as shown in Fig. 1(c). However, in practical applications, voids will coalesce before they come into contact with each other. Alternatively, there are failure mechanisms with only the void growth stage but not void coalescence, i.e., in the Orowan alternating slip mechanism, the void will grow self-similarly until the failure, without coalescence [5], as shown in Fig. 1(d). This study focuses on the most common mode of void coalescence by necking.

The present work aims to capture the ductile failure behavior in anisotropic FCC single crystals through the mechanism of void coalescence by necking. It is obtained through the following objectives: (i) To avoid spurious loading from partial RVE usage, i.e., capture full void cell to implement the multiaxial stress state accurately (ii) Enforce the multiaxial loading on the RVE using the simpler implementation of multipoint constraint (MPC) and load path parameters (T and L), i.e., using 6 node implementation of MPC than existing 4 node implementation (Tekoglu [43]). (iii) Detect the easier method to capture the onset of void coalescence by necking (iv) Investigate the role of void volume fraction, load path parameters, material anisotropy, crystal orientation, and its interplay on the void coalescence strain and morphology. The void coalescence strains estimated from this study will be useful for developing phenomenological models [13,44]. The novelty of the present work is to avoid spurious loading using six-noded MPC on a full RVE. Further, this study is the first of its kind to capture the effect of plastic anisotropy on the final void morphology and coalescence strain as a function of the slip system.

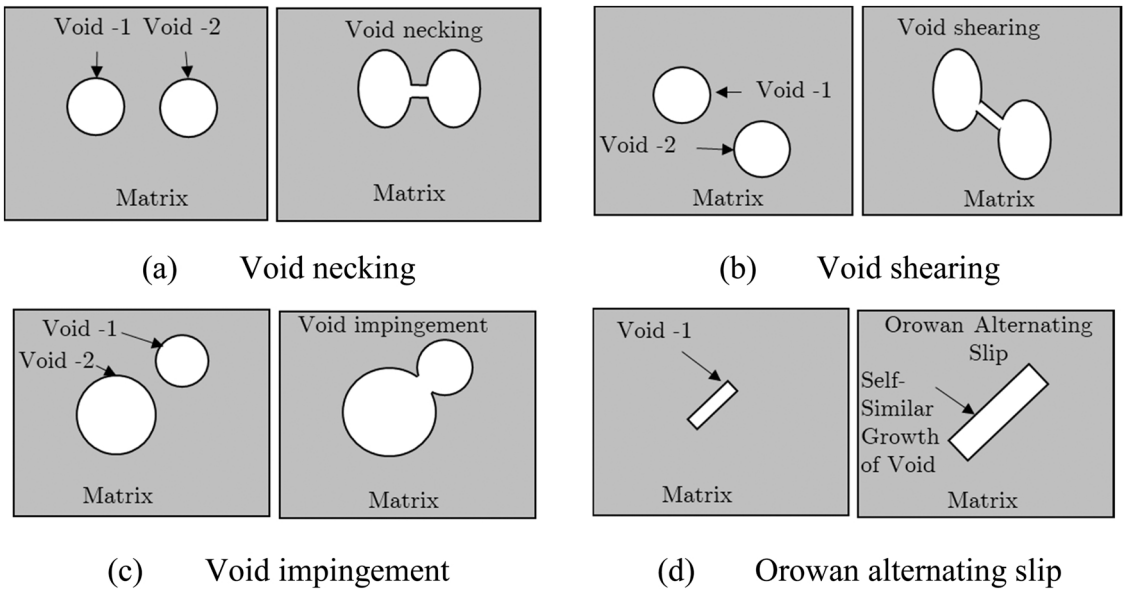

Fig. 1. Modes of ductile fracture (a-c) with void coalescence (d) without void coalescence.

This work investigates ductile failure through void necking for Cu single crystal. The remainder of the paper is organized as follows. Section 2 details the crystal plasticity framework and its implementation using the user subroutine in ABAQUS. Apart from the material model, the boundary value problem and implementation of constant load path parameters are also provided in Section 2. The effect of material anisotropy, load path parameters, and void volume fraction on the onset of void coalescence are presented in Section 3. Lastly, this study ends with major conclusions in Section 4.

2. Methodology

This section delineates the boundary value problem used to investigate the void coalescence (Section 2.1), the methodology to enforce the constant load path parameters (T and L) in Section 2.2, and the material model: crystal plasticity framework for the viscoplastic single crystal material (Section 2.3). Finally, a mesh convergence study was performed in Section 2.4 to obtain the optimum mesh size for the RVE.

2.1. Boundary value problem

The void coalescence through necking was studied in the present work using an RVE consisting of a 3D unit cell with a spherical void embedded at the center, as shown in Fig. 2. RVE-based simulations are generally used to investigate ductile fracture as a substitute for experiments to understand complex failure mechanisms [33–35,42]. Using the RVE-based design of experiments, the effect of geometric parameters (void size and shape), load path parameters (T and L), and material anisotropy (initial crystallographic orientations and slip systems) can be investigated systematically.

Earlier works used a one-eighth model of RVEs in their simulations, as they assumed greater material, loading, and geometric symmetry and were restricted to axisymmetric cases. However, the usage of one-eighth models cannot capture the anisotropy of the crystal [45]. This study presents the mechanistic modeling of deformation through a crystal plasticity framework to include anisotropy. Therefore, a full RVE model with periodic boundary conditions is used in the current work to incorporate the material, loading, and geometric anisotropy.

The details of the RVE used in this study, along with boundary conditions, are shown in Fig. 2. The initial side lengths of the RVE were $L_{10} = L_{20} = L_{30} = L_0$ and initial ligament lengths were of $LL_{10} = LL_{20} = LL_{30} = LL_0$, as shown in Fig. 2. A spherical void with an initial radius R_0 was embedded at the center of the RVE. The initial void volume fraction (f_0) of the RVE can estimated as

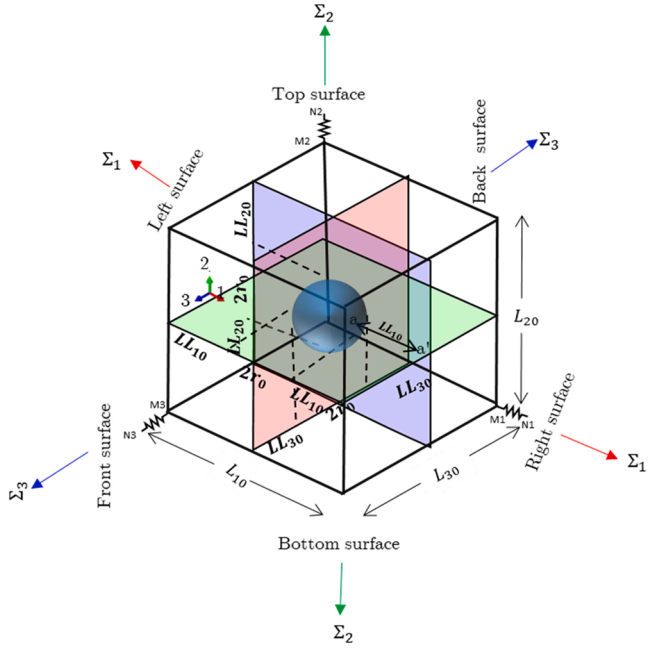

Fig. 2. Schematic of RVE used to study the void coalescence.

$$f_0 = \frac{4}{3}\pi\left(\frac{R_0}{L_0}\right)^3 \tag{1}$$

The macroscopic stresses ($\Sigma_1, \Sigma_2, \Sigma_3$) were applied on the faces of RVE with the help of displacements ($U_1^{M1}, U_2^{M2}, U_3^{M3}$) obtained from the multi-point constraint (MPC); see Section 2.2 for details. The boundary conditions applied on the faces of the RVE to maintain the constant load path parameters (T and L) are given below.

$$U_1^{Left} - U_1^{Right} = U_1^{M1}$$

$$U_2^{Top} - U_2^{Bottom} = U_2^{M2}$$
$$U_3^{Front} - U_3^{Back} = U_3^{M3} \quad (2)$$

Where in the displacement (i.e., U_1^{Left}, U_1^{M1}), subscript denotes the direction, and superscript denotes the face/node of the RVE. The equivalent macroscopic stress (Σ_{eq}) on the RVE is given by

$$\Sigma_{eq} = \frac{1}{\sqrt{2}}\sqrt{(\Sigma_1 - \Sigma_2)^2 + (\Sigma_2 - \Sigma_3)^2 + (\Sigma_1 - \Sigma_3)^2} \quad (3)$$

The equivalent macroscopic strain (E_{eq}) is given by

$$E_{eq} = \frac{\sqrt{2}}{3}\sqrt{(E_1 - E_2)^2 + (E_2 - E_3)^2 + (E_1 - E_3)^2} \quad (4)$$

Where the macroscopic logarithmic strains E_i were given by

$$E_1 = \ln\left(\frac{L_1}{L_{10}}\right);\ E_2 = \ln\left(\frac{L_2}{L_{20}}\right);\ E_3 = \ln\left(\frac{L_3}{L_{30}}\right) \quad (5)$$

Where $L_1 = L_{10} + U_1^{M1}; L_2 = L_{20} + U_2^{M2}; L_3 = L_{30} + U_3^{M3}$ were the current length of the cube sides.

It is observed from the literature that the onset of void coalescence is influenced by geometrical parameters (void size and shape) and load path parameters (T and L) [35,43]. Furthermore, from our previous study [45], it was found that f_0 and initial crystallographic orientation (ICO) significantly influences void evolution. Therefore, to study the effect of T, L, f_0, and ICO on the onset of void coalescence, a wide range of possible values were studied, as given in Table 1.

2.2. Enforcing constant load path parameters

Apart from imposing the periodic boundary conditions on RVE, it is required to maintain the constant load path parameters (T and L) to investigate their effect on the onset of void coalescence. This section explains the multi-point constraint (MPC) equations used to maintain the constant load path parameters and their implementation using a user subroutine in ABAQUS. Tekoglu [43] implemented with the help of three springs connecting four nodes; however, implementation with four nodes becomes complex, enhancing the chances of error. This study implemented constant load path parameters using three springs connecting six nodes, as shown in Fig. 2. Implementation with the help of six nodes and three springs maintains the symmetry of the model and is less complex in nature. The macroscopic stresses ($\Sigma_1, \Sigma_2\Sigma_3$) were applied on the faces of the RVE with the help of spring elements, as shown in Fig. 2. These applied macroscopic stresses were given by

Table 1
Factors influencing void coalescence and corresponding values used in this study.

SL No	Parameter	Values	Remarks
1	Stress triaxiality (T) [46]	$\frac{1}{3}, \frac{2}{3}$,1,2, and 3	(a) round bars: 0.3–0.5 (b) thin specimens: 0.5–0.8 (c) notched specimens: 0.5–1.5 (d) near the vicinity of crack: ~3
2	Lode parameter (L) [10]	-1, 0, and 1	(a) axisymmetric tension: −1 (b) plane strain: 0 (c) axisymmetric compression: 1
3	Initial void volume fraction (f_0)	0.005, 0.01 and 0.05	(a) voids due to secondary particles' decohesion and particle cracking: 0.005–0.05 (b) inherent voids: 0.005–0.05
4	Initial crystallographic orientation (ICO)	[100], [110], and [111]	(a) vertices of the standard stereographic triangle: [100], [110], [111] (a) four-fold symmetry: [100] (b) two-fold symmetry: [110]

$$\Sigma_1 = \frac{F_1}{A_{Right}};\ \Sigma_2 = \frac{F_2}{A_{Top}};\ \Sigma_3 = \frac{F_3}{A_{Front}} \quad (6)$$

Where $A_{Right}, A_{Top}, A_{Front}$ are the right, top, and front surface areas of the RVE, respectively, and given by

$$A_{Left} = A_{Right} = \left(L_{30} + U_3^{M3}\right)\left(L_{20} + U_2^{M2}\right)$$
$$A_{Top} = A_{Bottom} = \left(L_{30} + U_3^{M3}\right)\left(L_{10} + U_1^{M1}\right)$$
$$A_{Front} = A_{Back} = \left(L_{10} + U_1^{M1}\right)\left(L_{20} + U_2^{M2}\right) \quad (7)$$

The forces F_1, F_2, and F_3 applied on the faces of the RVE with the help of spring elements were given by

$$F_1 = K_{11}\Delta U_1; F_2 = K_{22}\Delta U_2; F_3 = K_{33}\Delta U_3 \quad (8)$$

Where $K_{11} = K_{22} = K_{33} = K$ are the spring constants of the springs between the node pairs M1-N1, M2-N2, and M3-N3, respectively, as shown in Fig. 2. The displacements imposed on the springs: $\Delta U_1 = U_1^{N1} - U_1^{M1}; \Delta U_2 = U_2^{N2} - U_2^{M2}$, and $\Delta U_3 = U_3^{N3} - U_3^{M3}$ were obtained from the MPC subroutine to maintain the constant load path parameters. The relationship between the imposed macroscopic stresses is given by ratios R_{11} and R_{33}, i.e.,

$$R_{11} = \frac{\Sigma_1}{\Sigma_2};\ R_{33} = \frac{\Sigma_3}{\Sigma_2} \quad (9)$$

The load path parameters (T and L) were defined as

$$T = \frac{\Sigma_h}{\Sigma_{eq}}; L = \frac{2\Sigma_2 - \Sigma_1 - \Sigma_3}{\Sigma_1 - \Sigma_3} \quad (10)$$

Where the hydrostatic stress Σ_h is given by $\Sigma_h = \frac{\Sigma_1+\Sigma_2+\Sigma_3}{3}$. From the above two equations (i.e., Eqs. 9 and 10), the expressions for load path parameters (T and L) in terms of ratios (R_{11} and R_{33}) were given by

$$T = \frac{\sqrt{2}(R_{11} + R_{33} + 1)}{3\sqrt{(1 - R_{11})^2 + (1 - R_{33})^2 + (R_{11} - R_{33})^2}};$$
$$L = \frac{1 + R_{11} - 2R_{33}}{1 - R_{11}} \quad (11)$$

To maintain the constant load path parameters (T and L), the ratios (R_{11} and R_{33}) should be kept constant as per Eq.11. To achieve this, Eq. 9 was modified with the help of Eqs. 6 and 8.

$$R_{11} = \frac{\Sigma_1}{\Sigma_2} = const \rightarrow \Delta U_1 - R_{11}\frac{A_{Right}}{A_{Top}}\Delta U_2 = 0$$
$$R_{33} = \frac{\Sigma_3}{\Sigma_2} = const \rightarrow \Delta U_3 - R_{33}\frac{A_{Front}}{A_{Top}}\Delta U_2 = 0 \quad (12)$$

For a given load path (i.e., a given ratios R_{11} and R_{33}), with varying vertical displacement on node N2 (U_2^{N2}), remaining displacements (U_1^{N1}, $U_1^{M1}, U_2^{M2}, U_3^{N3}, U_3^{M3}$) were obtained by satisfying the constraints in Eq. 12, using the MPC subroutine in ABAQUS. Different combinations of load path parameters (T and L) were attained by varying the values of ratios R_{11} and R_{33}. The various loading conditions and their corresponding R_{11} and R_{33} values are listed in Table 2. For further information on the implementation of constant load path parameters, one can refer to [43, 47].

2.3. Material model for viscoplastic single crystal

This study used the crystal plasticity framework to incorporate material anisotropy. Crystal plasticity models the deformation by explicitly considering homogeneous slip occurring at the microstructural level. This mechanistic approach accurately represents the triaxial boundary

Table 2
Values of R_{11} and R_{33} to attain different load path parameters (T and L).

Ratio R_{11}	Ratio R_{33}	Triaxiality (T)	Lode Parameter (L)
0.72	0.72	3	-1
0.677	0.838	3	0
0.7	1	3	1
0.625	0.625	2	-1
0.552	0.776	2	0
0.571	1	2	1
0.4	0.4	1	-1
0.268	0.634	1	0
0.25	1	1	1
0.25	0.25	0.67	-1
0.07	0.54	0.67	0
0	1	0.67	1
0	0	0.33	-1
-0.316	0.314	0.33	0
-0.5	1	0.33	1

condition and provides a realistic model to investigate void coalescence.

According to the multiplicative decomposition, the deformation gradient (F) was given by [48,49].

$$F = F^e.F^p \tag{13}$$

Where F^e is an elastic part of the deformation gradient consisting of elastic rotation and stretching, and F^p is a plastic part of the deformation gradient consisting of plastic spin and deformation. The constitutive behavior for the elastic part relating to Cauchy stress (σ) is given by

$$\sigma = C : D \tag{14}$$

Where C is the fourth-order elastic constant tensor; D is the Green-Lagrange strain tensor and is given by $\frac{1}{2}\left(F^{e^T}F^e - I\right)$; I is the fourth-order identity tensor. The velocity gradient is provided by

$$L^t = L^e + L^p = \left\{\dot{F}^e F^{e-1}\right\} + \left\{F^e \dot{F}^p F^{p-1} F^{e-1}\right\} \tag{15}$$

Where L^e and L^p are the elastic and plastic velocity gradients. The constitutive behavior for the plastic part is given by relating the velocity gradient with the shear strain rate ($\dot{\gamma}$)

$$L^p = \sum_\alpha \dot{\gamma}^\alpha (s^\alpha m^\alpha) \tag{16}$$

Where s^α, m^α are the slip direction and normal of the slip plane of the slip system α in the deformed configuration. In this study, void coalescence in Cu single crystal is investigated. The Cu single crystal has a face-centered crystal (FCC) structure with twelve slip systems defined by $\langle\bar{1}10\rangle\{111\}$. The evolution of shear rate ($\dot{\gamma}^\alpha$) is related to the resolved shear stress (τ^α) given by power law, as given below

$$\dot{\gamma}^\alpha = \dot{a}^\alpha \left(\frac{\tau^\alpha}{g^\alpha}\right)\left|\frac{\tau^\alpha}{g^\alpha}\right|^{n-1} \tag{17}$$

Where n, $\dot{a}^\alpha$ represents the slip rate sensitivity exponent and the reference strain rate on the slip system α, respectively. The resolved shear stress on the slip system (τ^α) is given by

$$\tau^\alpha = \sigma : sym(s^\alpha m^\alpha) \tag{18}$$

Where g^α is the current strength of the slip system, and it evolves with strain hardening, as given by Eq. 19.

$$g^\alpha = \sum_\beta h_{\alpha\beta}\dot{\gamma}^\beta \tag{19}$$

Where $h_{\alpha\beta}(\alpha \neq \beta) = qh_{\alpha\alpha}$ is the latent hardening modulus, β is activated slip systems. The self-hardening modulus $h_{\alpha\alpha}(\alpha = \beta)$ is given by Peirce, Asaro, and Needleman [50].

$$h_{\alpha\alpha} = h(\gamma) = h_0 \mathrm{sech}^2\left|\frac{h_0\gamma}{\tau_s - \tau_0}\right| \tag{20}$$

Where h_0 is the initial hardening modulus, τ_s is the stage-I stress, τ_o is the initial yield stress, and γ is the cumulative shear strain on all the slip systems and given by

$$\gamma = \sum_\alpha \int_0^t |\dot{\gamma}^\alpha| dt \tag{21}$$

The ABAQUS user material subroutine (UMAT) implements this complete finite-strain crystal plasticity framework. The material properties of the Cu single crystal used in this study are listed in Table 3 [49,50].

For more details on MPC implementation refer to Tekoglu's work [43] and the details of UMAT implementation refer to Huang's work [49]. The crystal plasticity framework is verified for the non-voided model Cu single-crystal model under a uniaxial tensile test with Huang [49]. After implementing MPC, results were verified whether constant load path parameters were maintained or not.

2.4. Mesh convergence study

The convergence of the FE simulations is influenced by the mesh density (i.e., element size). A coarse mesh will yield inaccurate results, while very-fine mesh incurs high computation costs. An optimal mesh with no appreciable change in the result with an increase in mesh density is preferable. In this study, the mesh convergence study was carried out using a full RVE model with $f_0 = 0.01$, ICO = [100] and the loading conditions of T = 1, L = −1, as shown in Fig. 2.

The RVE model was discretized with hexahedral elements (C3D8 in ABAQUS) with different mesh densities, as shown in Fig. 3. The crystal plasticity framework and constant stress triaxiality were employed with the help of UMAT and MPC subroutine in ABAQUS. Simulations were performed by increasing the mesh density; the predicted results were plotted with the following mesh densities: 1016, 2528, 3728, 5120, and 7632 elements.

As the first step of mesh convergence, the applied equivalent stress (Σ_{eq}) vs. equivalent strains (E_{eq}) was compared in Fig. 4 for different mesh densities. The inset picture in Fig. 4 shows the enlarged view of strain values ranging from 0.1 to 0.2 along the x-axis and corresponding stress values. The inset figure shows that the model with 1016 elements is clearly deviating from the rest of the models and indicating huge convergence issues. Other than the 1016 elements model, all models predict similar stress-strain curves.

Further, the displacement along the Y-direction (U2) at the periphery of the spherical void (highlighted in a red circle in Fig. 3) with respect to equivalent strain was given in Fig. 5. The models with 5120 and 7632 elements showed the same results; the difference between the results of these models is less than one percent, but the time taken is 1.5 times more for the case 7632 elements. Similar convergence was observed for the f_0 = 0.005, 0.05. Therefore, the model with 5120 elements was chosen for the simulations.

3. Results and discussion

In this section, the results of ductile failure by void coalescence

Table 3
Cu single crystal material properties.

Elastic properties			Plastic properties					
C_{11} (GPa)	C_{12} (GPa)	C_{44} (GPa)	n	$\dot{a}^\alpha$	h_0 (MPa)	τ_o (MPa)	τ_s (MPa)	q
168.4	121.4	75.4	10	0.001	514.5	60.8	109.5	1

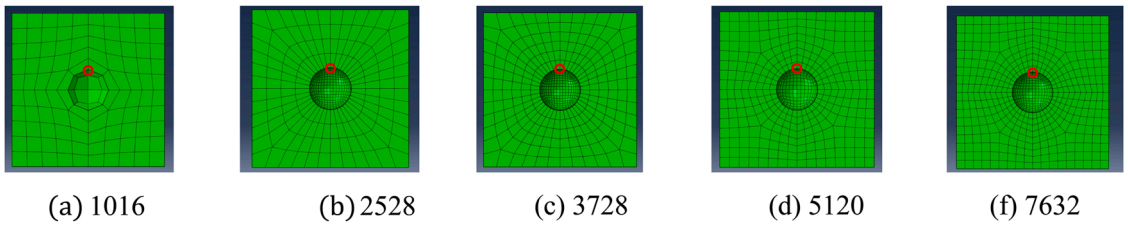

Fig. 3. Cross section of the RVE at midplane along direction-1 for different element size.

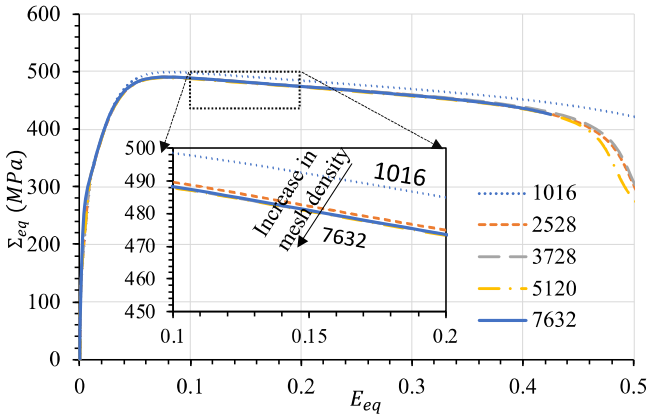

Fig. 4. Equivalent stress vs. strain graph for different mesh sizes for $f_0 = 0.01$, ICO = [100], and the loading conditions of T = 1, L = −1.

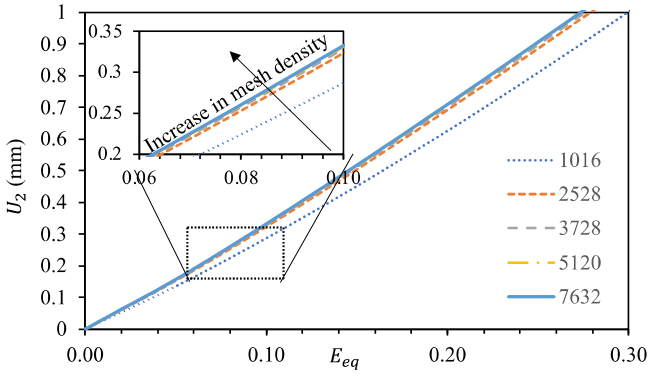

Fig. 5. Vertical displacement U2 vs. strain graph for different mesh sizes for $f_0 = 0.01$, ICO = [100], and the loading conditions of T = 1, L = −1.

through necking in Cu single crystal are discussed in detail. Here, methods to identify the onset of void coalescence and load path influence on the coalescence are presented in Section 3.1. The effect of material anisotropy on void coalescence is detailed in Section 3.2. The size effects of initial spherical void size (R_0) and ligament length (LL_0) in terms of f_0 on the onset of void coalescence are described in Section 3.3. The void morphology at the onset of void coalescence is presented in Section 3.4, as it decides the final form of the coalesced void. Finally, the effect of the Lode parameter is presented in Section 3.5.

3.1. Void coalescence under tensile loading

The onset of void coalescence is not straightforward to pinpoint from the stress-strain curve during ductile failure. In general, the onset of void coalescence is identified by different approaches, such as loss of load-bearing capacity, transition to uniaxial straining mode, a rapid rise in void volume (f), and thinning down of ligament length (LL→0) [46,51]. All these approaches to identify the onset of void coalescence are presented in this section in detail for Cu single crystal.

The equivalent macroscopic stress (Σ_{eq}) vs. strain (E_{eq}) curves were generated for the several load path parameters (T and L) applied on the RVE (see Section 2.1) using the multi-point constraints described in Section 2.2 for the material model presented in Section 2.3. The equivalent stress (Σ_{eq}) and strain E_{eq} were calculated from the Eq. 3 and Eq. 4, respectively for every increment the vertical displacement of node N_2 (U_2^{N2}). Fig. 6(a) illustrates the Σ_{eq} vs. E_{eq} for Cu single crystal RVE with $f_0 = 0.01$ and ICO = [100] under various tensile loading (L = −1, $\frac{1}{3} \leq T \leq 3$). Tensile loading (L = −1) leads to void growth and causes void coalescence, whereas other cases (i.e., L = 0 and 1) lead to void shrinkage and collapse [26]. For other cases (i.e., ICO = [110], [111], f_0 = 0.001, 0.005, L = −1), similar trends were observed, not shown here for brevity.

The stress-strain curves in Fig. 6(a) increase linearly to reach their peak value, then drop down. The slope of the stress-strain curve in the elastic region is approximately the same for all the triaxial (T) loading conditions. However, the peak stress value decreased with an increase in T. Post peak shows the fall in the stress-strain curve, indicating the material softening due to the void growth. The decrease in the slope of the post-peak curve is rapid for high triaxial values (T∼3) and slow for low triaxial values (T = 0.33). The drop in slope indicates the rate at which the material loses its load-bearing capacity. The sharp knee in the stress-strain curve represents the void coalescence and is denoted by black open circles in Fig. 6(a). The sharp knee in the stress-strain curve was discernible for the case of high triaxialities, whereas at low triaxial values, it cannot be captured clearly.

Fig. 6(b) describes the plot between logarithmic strain along direction-1 (E_1) and equivalent strain (E_{eq}) for the same loading conditions discussed in Fig. 6(a). The logarithmic strain E_1 were calculated from the Eq. 5 in Section 2.1. With increase in E_{eq} a linear increment in logarithmic strain E_1 was observed till a critical equivalent strain (E_{eqc}), beyond which E_1 stayed constant. In other words, above E_{eqc} there was saturation in E_1, hence E_{eq} vs. E_1 became horizontal. This E_{eqc} represents the onset of void coalescence beyond which the deformation mode completely changes to uniaxial straining. This event of a change in deformation mode is the void coalescence, marked with a black open circle in Fig. 6(b).

Fig. 6(c) depicts the graph between the ratio of the current void volume fraction (f) to initial void volume fraction (f_0) and equivalent strain (E_{eq}) for the various loading conditions discussed in Fig. 6(a). The current void volume fraction (f) was calculated by subtracting the matrix volume (summation over all integration point volumes) from the volume of the cube ($L_1 \times L_2 \times L_3$). A similar method was used by Karanam et al. [45] for calculating f. With an increase in E_{eq}, there is a rise in the void volume fraction ratio because of the tensile loading. Initially, the slope of the curve is less; later, there is a sudden rise in the void volume, which denotes the onset of void coalescence. The event of the sudden rise in slope from low value to high indicates the onset of void coalescence.

The geometric means of identifying the void coalescence is by the thinning down of the ligament length (LL→0). Thomason's [52] criteria for the onset of void coalescence is based on the plastic limit load in the ligament length. Fig. 6(d) denotes the plot between the ratio of ligament

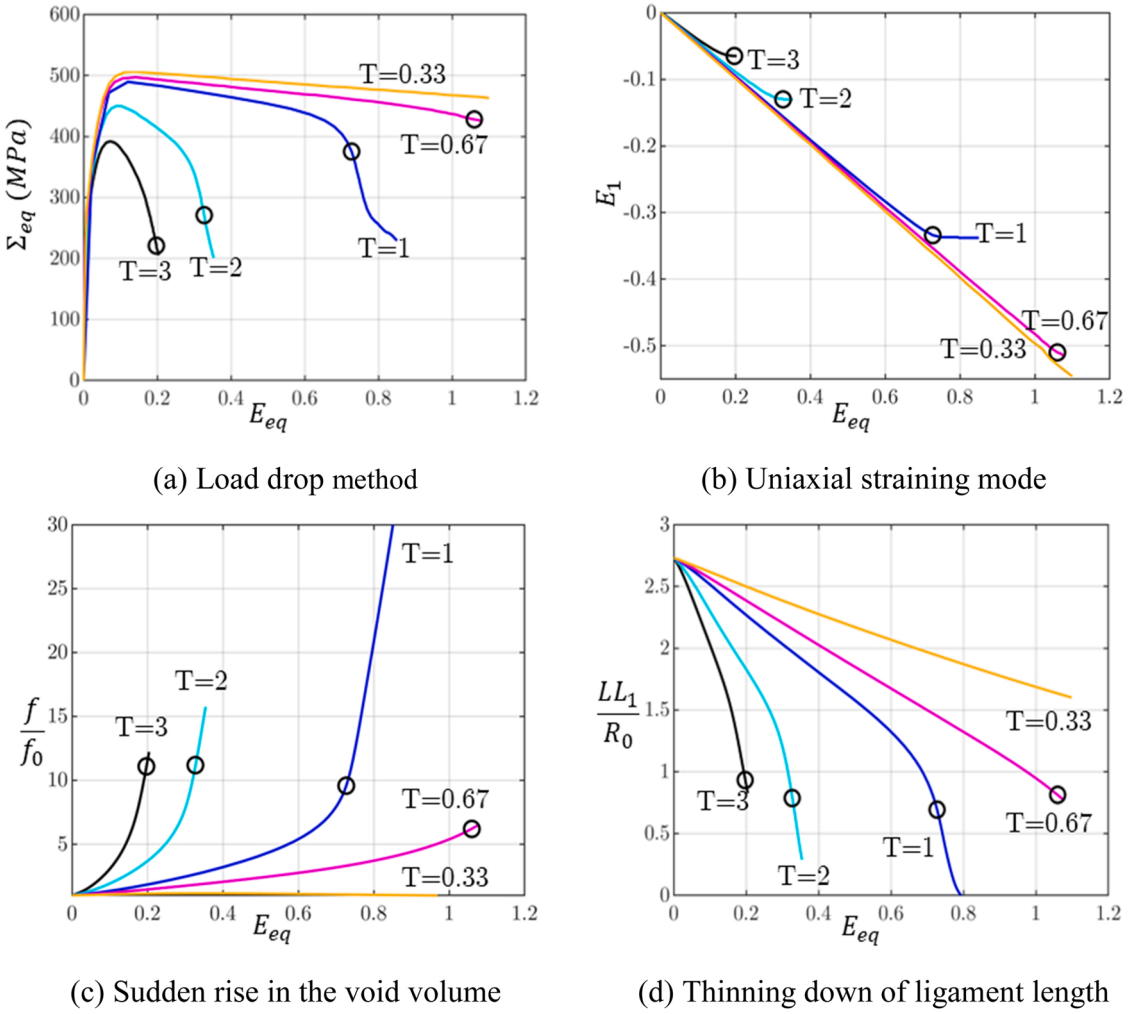

(a) Load drop method (b) Uniaxial straining mode

(c) Sudden rise in the void volume (d) Thinning down of ligament length

Fig. 6. Void coalescence at different T for ICO= [100], L= -1, f_0= 0.01.

length in the direction-1 to the initial void radius ($\frac{LL_1}{R_0}$) and equivalent strain (E_{eq}), for the various loading conditions discussed in Fig. 6(a). The ligament length LL_1 was calculated by subtracting the relative displacement between the two nodes (a-a′) from LL_{10}, see Fig. 2. With an increase in E_{eq}, there is a linear drop in the curve, after reaching critical value, the drop was rapid. This point is denoted as the onset of void coalescence. The strain at which void coalescence starts (E_{eqc}) was approximately the same as all four methods discussed above. However, the deformation transition to uniaxial mode (Fig. 6(b)) is less ambiguous than the remaining methods. Therefore, Fig. 6(b) is widely used to identify the onset of void coalescence in unit cell simulations [33]. The obtained void coalescence strain (E_{eqc}) from Fig. 6(b) and corresponding Σ_{eq}, $\frac{f}{f_0}$, and $\frac{LL_1}{R_0}$ were marked with a black open circle in Fig. 6(a,c,d), respectively. It is observed that void coalescence occurs earlier in the case of high triaxial values compared to low triaxialities.

Fig. 3(a-d) shows that there is a rapid decrease in coalescence strains (E_{eqc}) with an increase in triaxiality. During the deformation under tensile loading, two main events happen a) strain hardening of the material and b) material softening due to void growth. The interplay between these critical events decides the material behavior of RVE. Once the material softening due to the void growth dominates, a sudden drop in the load-carrying capacity of the material is observed, leading to void coalescence. The rapid void growth at high triaxial loads leads to coalescence at earlier strains. Rice & Tracy [14] and Zhu et al. [53] made a similar observation; they showed that coalescence strain decreases exponentially with increased triaxiality. For T = 0.33, these methods cannot capture coalescence clearly. For T = 0.33 & L = -1, transition to uniaxial deformation is not observed, as loading itself represents the pure uniaxial. Moreover, at low triaxial values, the voids will coalesce by shearing mode (see Fig. 1(b)), similar to the observations of [16,43,54].

3.2. Void coalescence dependence on material anisotropy

The influence of material anisotropy on the onset of void coalescence is presented in this section. The ICOs [100], [110], and [111] were investigated, as these orientations represent vertices of the standard stereographic triangle. Fig. 7(a&b) shows the plot between the macroscopic stress (Σ_{eq}) vs. strain (E_{eq}) of Cu single crystal RVE with $f_0 = 0.01$ under tensile loading (L = -1) for the cases of high triaxiality (T = 3) and medium triaxiality (T = 1), respectively. For Fig. 7, the void coalescence was identified by the transition to uniaxial mode on the strain plot (like Fig. 6(b)) and indicated with a black open circle. Low triaxiality is not presented as it is difficult to capture the void coalescence for T < 1. The above simulation results show that ICO = [111] has the highest peak stress (Σ_{eqp}) compared to the remaining two ICOs ($\Sigma_{eqp}^{[111]} > \Sigma_{eqp}^{[110]} > \Sigma_{eqp}^{[100]}$). The onset of void coalescence strain (E_{eqc}) is highest for the ICO = [110] compared to the remaining two ICOs ($E_{eqc}^{[110]} > E_{eqc}^{[100]} > E_{eqc}^{[111]}$). It is to be noted that though ICO = [110] showed the medium peaks stress, it has the highest ductility among all other orientations considered, i.e., void coalescence strains were high. The highest Σ_{eqp} for ICO = [111] is attributed to its high material hardening, and lowest Σ_{eqp}

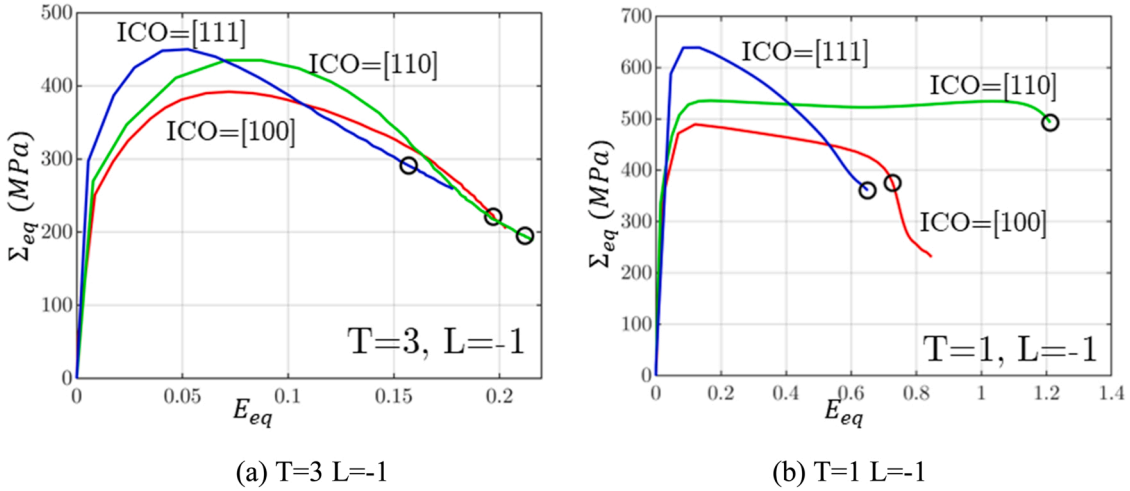

(a) T=3 L=-1 (b) T=1 L=-1

Fig. 7. Material anisotropy effect on coalescence.

for ICO = [100] is attributed to its low material hardening caused by the favorable slip systems.

In Fig. 7, the differences between the highest and lowest void coalescence strains ($E_{eqc}^{[110]} - E_{eqc}^{[111]}$) for various ICOs considered are around 0.05 for high triaxiality (T = 3) and 0.6 for medium triaxiality (T = 1), respectively. These differences are more than ten times for

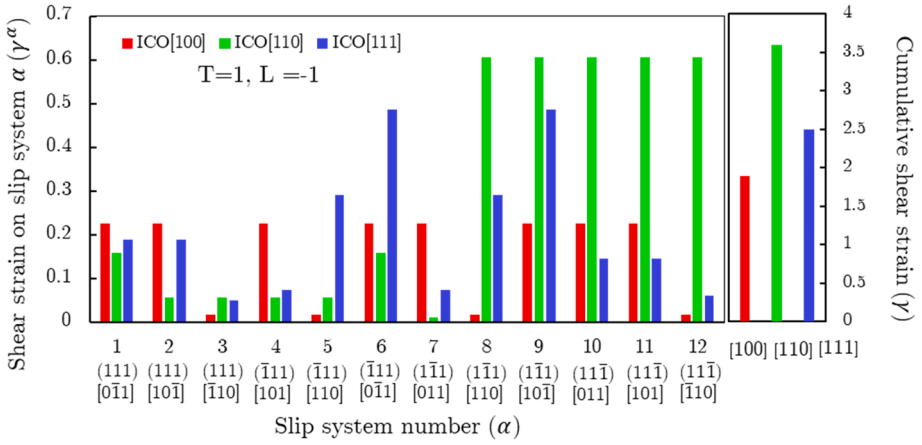

(a) Shear strain on each slip system ($\boldsymbol{\gamma^\alpha}$) and cumulative shear strain ($\boldsymbol{\gamma}$) at the onset of coalescence T=1; L =-1; $\boldsymbol{f_0}$ = 0.01

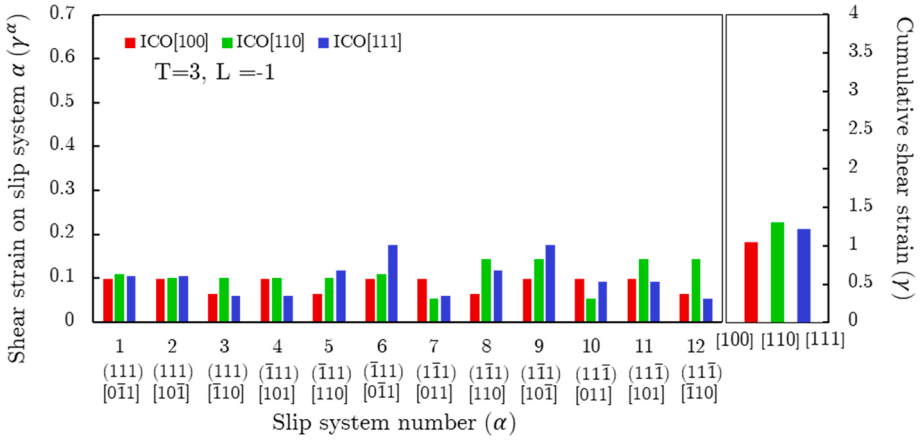

(b) Shear strain on each slip system (γ^α) and cumulative shear strain (γ) at the onset of coalescence T=3; L =-1; $\boldsymbol{f_0}$ = 0.013

Fig. 8. (a) Shear strain on each slip system (γ^α) and cumulative shear strain (γ) at the onset of coalescence T = 1; L = −1; f_0 = 0.01. (b) Shear strain on each slip system (γ^α) and cumulative shear strain (γ) at the onset of coalescence T = 3; L = −1; f_0 = 0.013.

medium triaxiality compared to high triaxiality. It indicates that the dependence of void coalescence strain on initial crystallographic orientation is less at high triaxiality (T = 3) and significantly increases with a decrease in triaxiality.

Fig. 8(a & b) shows the shear strain on the slip system α (γ^{α}) on each of the 12 slip systems for three different ICOs, along with the cumulative shear strain (γ) for different ICOs at the onset of void coalescence for T = 1, 3, respectively at L = −1; f_0 = 0.01. In Fig. 8(a), the cumulative shear strain exhibits the following trend $\gamma_{[110]} > \gamma_{[111]} > \gamma_{[100]}$. It is observed that the shear strain on each slip system (γ^{α}) for ICO = [110] is high for slip systems $(1\bar{1}1)[110]$, $(1\bar{1}1)[10\bar{1}]$, $(11\bar{1})[011]$, $(11\bar{1})[101]$, $(11\bar{1})[\bar{1}10]$ than other slip systems. This is because these five slip systems are more favorable for the slip than other slip systems. The combined effect of these five slip systems contributed to more ductility of ICO = [110] than other orientations. Similarly, in ICO = [111], slip systems $(\bar{1}11)[110]$, $(\bar{1}11)[0\bar{1}1]$, $(1\bar{1}1)[110]$, and $(1\bar{1}1)[10\bar{1}]$ have higher contribution than other slip systems; hence the total cumulative shear is more than ICO = [100].

Guo and Li's [55] study on 5083-H116 aluminum alloy showed the highest peak stress for ICO = [111] ($\Sigma_{eqp}^{[111]}$), which is similar to our study. Whereas the highest ductility is for ICO = [100] ($E_{eqc}^{[100]}$), different from our study ($E_{eqc}^{[110]}$). A similar study on BCC single crystal was performed by Yerra et al. [35] and found that the highest peak stress for ICO = [110] and highest ductility ICO = [100]. Therefore, the effect of anisotropy on ductility significantly increases with a decrease in T. Fig. 8 (b) shows the individual shear strain on slip planes and cumulative shear strain on the slip system for T = 3. It is observed that the shear strains are much lower (~0.15) for T = 3 compared to T = 1. It is an indication that at high triaxiality, the necking is dominating phenomenon; as the triaxiality decreases, shear deformation comes into the picture apart from the necking. At very low triaxial values, shear deformation dominates.

Fig. 9 summarizes the void coalescence strains (E_{eqc}) for varying triaxiality under different material orientations. It can be seen that the void coalescence strains (E_{eqc}) in tensile loading (L = −1) decrease rapidly with an increase in triaxial value, as shown in Fig. 9. Material orientation effects the E_{eqc} significantly at low triaxial values. Material anisotropy effect on E_{eqc} is less significant at high triaxial value. Our estimations are qualitatively inline with the multi-surface model proposed by Vishwakarma and Keralavarma (see Fig 15 of [56]); quantitative comparison is not possible because of the different material models used.

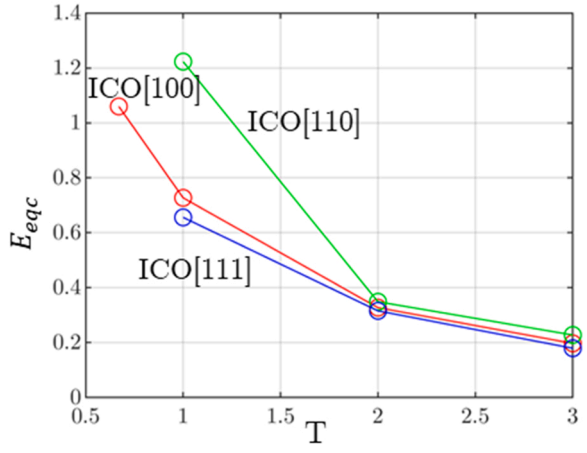

Fig. 9. Fracture locus for Cu with f_0 = 0.01, L = −1.

3.3. Void coalescence dependence on the initial void volume fraction

To study the effect of f_0 on the onset of void coalescence, three values of f_0 (0.005, 0.01, 0.05) were considered (see Table 1), and the results were discussed in this section. Fig. 10(a) shows the plot between the equivalent macroscopic stress (Σ_{eq}) vs. strain (E_{eq}) for the different f_0 values considered under tensile loading with T = 3 and ICO = [100]. A high triaxial value (T = 3) is shown here; at high triaxial values rise in void volume is high (see Fig. 6(c)), and the effect of f_0 can be studied clearly. The ICO = [100] is chosen because of its high symmetry compared to other ICOs. In Fig. 10(a), the stress-strain curve increases linearly, reaches its peak value, and drops down. It is observed that the highest f_0 (0.05) has the lowest Σ_{eqp}, and with the decrease in f_0 there is an increase in Σ_{eqp}. It is because the higher f_0 the lower the available material to resist the loads. Therefore, the material softening due to the void growth is higher for f_0 = 0.05, causing it to have the lowest Σ_{eqp}. The onset of the void coalescence is identified as discussed in Fig. 6(b), denoted with black open circles. It is found that the void coalescence strain (E_{eqc}) decreases with an increase in f_0, i.e., $E_{eqc}(0.005) > E_{eqc}(0.01) > E_{eqc}(0.05)$. The size of the void in higher f_0 is bigger, material softening to void is high, leading to coalesce at earlier strains.

Fig. 10(b) shows the plot between the ratio of the current void volume fraction to the initial void volume fraction ($\frac{f}{f_0}$) and equivalent strain (E_{eq}) for the same conditions discussed in Fig. 10(a). There is a rise in $\frac{f}{f_0}$ with an increase in E_{eq}, i.e., initially the rise is slow; later, the rise is rapid. Initially, the hardening behavior of the material makes it challenging to increase the void volume, hence the rise in $\frac{f}{f_0}$ is slow. Later, material softening due to void growth dominates, hence the rise in $\frac{f}{f_0}$ is rapid. The rise in the slope of the curve is higher for the small f_0 (0.005) compared to the remaining f_0 (0.01, 0.05). The rise in $\frac{f}{f_0}$ with an increase E_{eq} is exponential for low f_0 (0.005,0.01) and it is almost linear for the case of high f_0 (0.05).

3.4. Void morphology at void coalescence

The final form of the coalesced void gives the details on the mode of coalescence. This section presents void morphology at the onset of void coalescence.

Fig. 11 shows the cumulative shear strain (γ) contours at the onset of the void coalescence of RVE with f_0 = 0.01, ICO = [100] under tensile loading (L = −1, $\frac{2}{3} \leq T \leq 3$). These cumulative shear strain plots were obtained by cutting the RVE at the midplane along the direction-1 (see Fig. 2). At high triaxial values (T = 3), the shear strain was localized around the void periphery, expediting the void growth process. At low triaxial values (T = 0.67), the shear strain was distributed over the entire crystal, hindering the void growth process. It is observed that the void grows into an oblate shape at high triaxial values and a prolate shape at low triaxial values. Budiansky et al. [57] studied the asymptotic geometries of initially spherical voids (see Figure 3.1(a) of [40]) and found a similar observation for linearly viscous materials. Further, the oblate sphere shapes at high triaxiality depend on the material anisotropy; a detailed description of the void shape at the onset of void coalescence is presented in the following paragraph.

Fig. 12 shows the final coalesced void shape for oblate voids (T = 3, L = −1) for f_0 = 0.01. These plots were obtained at the onset of void coalescence by cutting the RVE with the help of cutting planes (i.e., plane-1, plane-2, and plane-3). The cutting planes are the midplanes along direction-1,2 and 3, respectively, as shown in Fig. 2. Here, each sub-figure consists of four images representing the void shape on plane-3, plane-1, plane-2, and the final void form in the clockwise order starting from the bottom left image (i.e., plane-1), respectively. Karanam and Chinthapenta [58] characterized the void shapes based on diagonal distortion and shape parameters; similar nomenclature is used here to

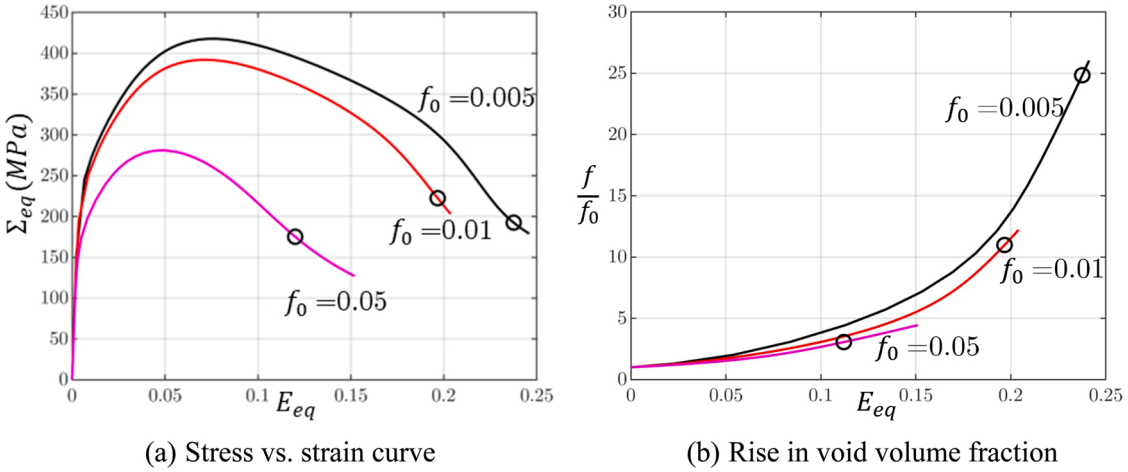

Fig. 10. Effect of f_0 on void coalescence for T = 3, L = −1, ICO = [100].

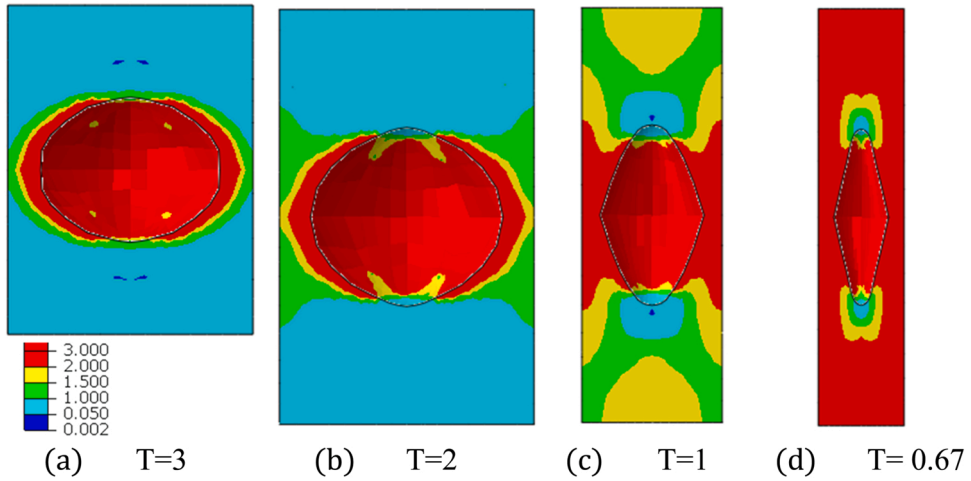

Fig. 11. Cumulative shear strain at the onset of void coalescence for ICO = [100], L= −1.

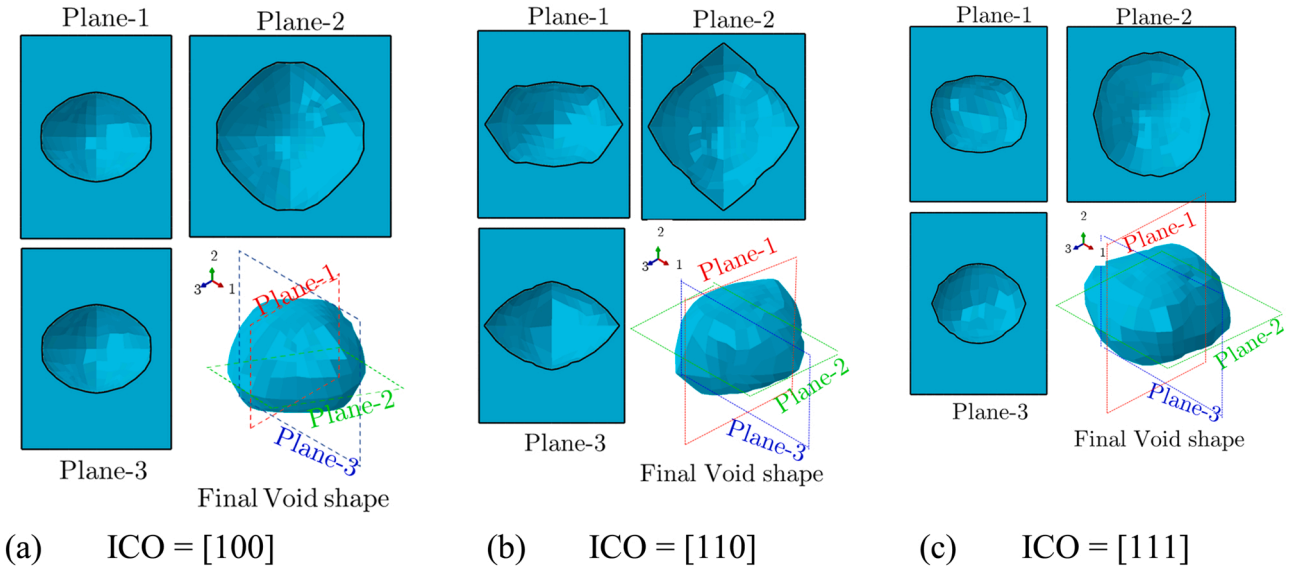

Fig. 12. Void shape at coalescence for different crystal orientations for T = 3, L= −1.

present the void shape (see Fig. 11 of [58]). The final void shape of the ICO = [100] has an oblate shape in plane-1 and plane-3 and a diamond shape in plane-2. Whereas ICO = [110] has a hexagonal shape in plane-1, a rhombus shape in plane-2, and an ellipse shape in plane-3. ICO = [111] has an oblate spin in plane-1, a super spheroidal shape in plane-2, and an oblate shape in plane-3. From the previous section (Section 3.2), it is found that at high triaxiality, material anisotropy has less effect on coalescence strain (E_{eqc}). However, it is found that it has a profound effect on the shape of the final coalesced void.

3.5. Effect of the tensile, plane strain, and compressive loading on coalescence

Fig. 13 shows the plot between the logarithmic strains E_1 and E_{eq} for different Lode parameters (L = −1, 0, 1) on Cu single crystal RVE with f_0 = 0.01 at T = 3, Remaining f_0 and T values were not presented for brevity. Fig. 13 illustrates the effect of the Lode parameter on the deformation and onset of void coalescence. In the figure, L = −1, 0, and 1 are denoted with an asterisk, triangle, and square markers, respectively. The crystallographic orientations ICO = [100], [110], and [111] are marked with red, green, and blue colors, respectively. The curves in the figure change linearly with an increase in E_{eq} until it reaches a saturated value. After the saturated value, the curves become parallel to the horizontal axis, indicating void coalescence. These void coalescence points are marked with black open circles in the figure.

Among the considered Lode parameters, L = −1 has the lowest slope compared to 0 and 1. The lower the slope of the curve, the simpler it is to attain saturation and become horizontal. The void coalescence is observed for L = −1, whereas coalescence is not observed for L = 0 and 1. This is because L = −1 causes the void growth that leads to coalescence, whereas L = 0 and 1 causes the void shrinkage that leads to collapse. This method is useful in detecting the void coalescence by necking, i.e., L = −1. The effect of crystal orientation significantly changes with a change in Lode parameter values. At L = −1, ICO = [100] has less slope, followed by [111] and finally [110]. Whereas for L = 0 and 1, ICO = [111] has less slope, followed by [100] and finally [110]. With the change in the Lode parameter value, the effect of material anisotropy is significant on the deformation behavior.

4. Conclusions

Void coalescence in Cu single crystal was investigated using a full RVE with periodic boundary conditions. The spurious loading condition caused by the use of a one-eighth model by assuming the greater symmetry was overcome with the use of full RVE. Material anisotropy arising from the orientation and slip phenomenon was captured using the crystal plasticity framework. To study the effect of the load path on void coalescence, constant load path parameters were imposed on the RVE with the help of a 6-node multi-point constraint implementation. The crystal plasticity framework and multi-point constraint were implemented through the user subroutines in ABAQUS to capture the material anisotropy.

Void coalescence criterion was identified using: (i) load carrying capacity, (ii) transition to uniaxial mode, (iii) rise in void volume fraction, and (iv) thinning down ligament length. It was found that the shift in deformation to uniaxial straining mode was less ambiguous among all the methods explored in this study. The quantitative measure for detecting void coalescence (E_{eqc} *or* f_c) were reported. The investigation of the triaxiality effect on void coalescence under tensile loading (L = −1) revealed that void coalescence strains (E_{eqc}) and peak stress (Σ_{eqp}) were low for the high triaxial loading. On the other hand, low triaxial loading showed higher ductility and peak stress (higher E_{eqc} & Σ_{eqp}), i.e., $E_{eqc(T=0.67)} - E_{eqc(T=3)} \sim 0.81$.

The effect of initial crystallographic orientation on E_{eqc} was less at high triaxial values ($E_{eqc}^{[110]} - E_{eqc}^{[111]} = 0.05$). Whereas at low triaxial values, the effect of material anisotropy was significant on E_{eqc}($E_{eqc}^{[110]} - E_{eqc}^{[111]} = 0.6$). The cumulative shear strain plot (see Fig. 8) revealed that slip systems $(1\bar{1}1)[110]$, $(1\bar{1}1)[10\bar{1}]$, $(11\bar{1})[011]$, $(11\bar{1})[101]$, $(11\bar{1})[\bar{1}10]$ were more favorable for the slip in the case of ICO = [110], causing it to have higher ductility. The interplay between triaxiality and material orientation revealed that E_{eqc} decreases rapidly with an increase in triaxial value, irrespective of the orientation.

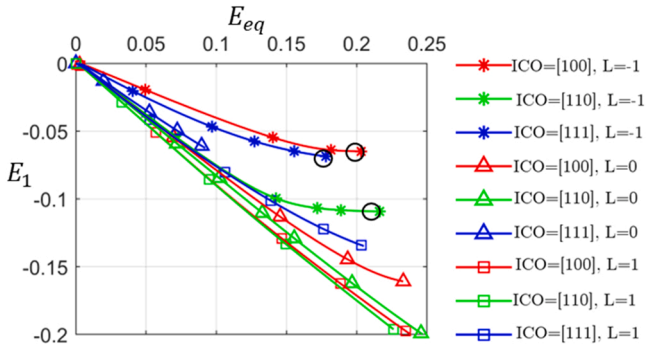

Fig. 13. Logarithmic strain E_1 Vs. E_{eq} for T = 3.

At the onset of void coalescence, the void shape changes from oblate to prolate with a decrease in triaxial values for the tensile loading cases (L=−1). At high triaxial values, material anisotropy has less effect on E_{eqc}, whereas it strongly influences the final shape of the void at the onset of coalescence. The initial void size (f_0) influences the E_{eqc} such that coalescence occurs at an earlier strain in the case of higher f_0, i.e., $E_{eqc}(0.05) < E_{eqc}(0.01) < E_{eqc}(0.005)$. The rise in void volume (f) was higher for lower f_0 and vice versa. The Lode parameter L = −1 represents the tensile loading that leads to void growth and coalescence. Whereas L = 0 and 1 illustrate the void shrinkage that leads to void collapse.

Though this study focused on Cu single crystal, it can be applied to any FCC material. However, extending this study to BCC crystal requires to rework on the slip system, as BCC has an entirely different slip system than FCC. The estimated coalescence strains provide useful insights into developing the anisotropic phenomenological models and are also useful in calibrating the existing phenomenological models, such as the modified GTN model. The limitation of the present study is that it can not induce the shear loads and can not capture coalescence under the shear mode, which is part of the future study.

CRediT authorship contribution statement

Gulivindala Gopi: Methodology, Software, Visualization, Writing-Original draft, **Madhu Kiran Karanam**: Investigation, Writing-Reviewing, **Kwong Ming Tse**: Validation, Funds, Writing- Reviewing, **Viswanath Chinthapenta**: Conceptualization, Visualization, Supervision, Funds, Writing- Reviewing.

Declaration of Competing Interest

The authors declare that they have no known competing financial interests or personal relationships that could have appeared to influence the work reported in this paper.

Data availability

Data will be made available on request.

Acknowledgment

Author GG acknowledges the MoE fellowship (2021–2022) from IIT

Hyderabad, India. Author VC would like to acknowledge the funding from Dassault systems foundation, India (La fondation) under grant number IN-2019-001.

References

[1] J. Kim, X. Gao, T.S. Srivatsan, Modeling of void growth in ductile solids: effects of stress triaxiality and initial porosity, Eng. Fract. Mech. 71 (2004) 379–400, https://doi.org/10.1016/S0013-7944(03)00114-0.

[2] J.A. Sharon, K. Hattar, B.L. Boyce, L.N. Brewer, Compressive properties of ⟨110⟩ Cu micro-pillars after high-dose self-ion irradiation, Mater. Res Lett. 2 (2014) 57–62, https://doi.org/10.1080/21663831.2013.859179.

[3] P.F. Weinrich, I.E. French, The influence of hydrostatic pressure on the fracture mechanisms of sheet tensile specimens of copper and brass, Acta Metall. 24 (1976) 317–322, https://doi.org/10.1016/0001-6160(76)90006-7.

[4] K.E. Puttick, Ductile fracture in metals, Philos. Mag. 4 (1959) 964–969, https://doi.org/10.1080/14786435908238272.

[5] E. Orowan, Fracture and strength of solids, Rep. Prog. Phys. 12 (1949) 185–232.

[6] P.J. Noell, J.D. Carroll, B.L. Boyce, The mechanisms of ductile rupture, Acta Mater. 161 (2018) 83–98, https://doi.org/10.1016/j.actamat.2018.09.006.

[7] J.I. Bluhm, R.J. Morrissey. Fracture in a tensile specimen, Technical Report, Army materials research agency, Watertown, MA, 1966.

[8] S. Ward, C. Braithwaite, A. Jardine, The dynamic ductile fracture of high purity copper. AIP Conf Proc vol. 1979, American Institute of Physics Inc., 2018, https://doi.org/10.1063/1.5044841, p. 070032–1-5.

[9] P.J. Noell, J.E.C. Sabisch, D.L. Medlin, B.L. Boyce, Nanoscale conditions for ductile void nucleation in copper: vacancy condensation and the growth-limited microstructural state, Acta Mater. 184 (2020) 211–224, https://doi.org/10.1016/j.actamat.2019.11.022.

[10] I. Barsoum, J. Faleskog, Micromechanical analysis on the influence of the Lode parameter on void growth and coalescence, Int J. Solids Struct. 48 (2011) 925–938, https://doi.org/10.1016/j.ijsolstr.2010.11.028.

[11] I. Barsoum, J. Faleskog, Rupture mechanisms in combined tension and shear-experiments, Int J. Solids Struct. 44 (2007) 1768–1786, https://doi.org/10.1016/j.ijsolstr.2006.09.031.

[12] S.H. Goods, L.M. Brown, the nucleation of cavities by plastic deformation. Perspectives in Creep Fracture, Elsevier,, 1983, pp. 71–85, https://doi.org/10.1016/b978-0-08-030541-7.50007-2.

[13] A.L. Gurson, Continuum theory of ductile rupture by void nucleation and growth: part I-Yield criteria and flow rules for porous ductile media, J. Eng. Mater. Technol. 99 (1977) 2–15, https://doi.org/10.1115/1.3443401.

[14] J.R. Rice, D.M. Tracey, on the ductile enlargement of voids in triaxial stress fields, J. Mech. Phys. Solids 17 (1969) 201–217, https://doi.org/10.1016/0022-5096(69)90033-7.

[15] Y. Huang, Accurate dilatation rates for spherical voids in triaxial stress fields, J. Appl. Mech. 58 (1991) 1084–1086, https://doi.org/10.1115/1.2897686.

[16] T. Pardoen, J.W. Hutchinson, An extended model for void growth and coalescence, J. Mech. Phys. Solids 48 (2000) 2467–2512, https://doi.org/10.1016/S0022-5096(00)00019-3.

[17] V. Tvergaard, On localization in ductile materials containing spherical voids, Int J. Fract. 18 (1982) 237–252, https://doi.org/10.1007/BF00015686.

[18] C.C. Chu, A. Needleman, Void nucleation effects in biaxially stretched sheets, J. Eng. Mater. Technol. 102 (1980) 249–256, https://doi.org/10.1115/1.3224807.

[19] V. Tvergaard, Influence of voids on shear band instabilities under plane strain conditions, Int. J. Fract. 17 (1981) 389–407, https://doi.org/10.1007/BF00036191.

[20] M. Gologanu, J.B. Leblond, J. Devaux, Approximate models for ductile metals containing non-spherical voids-case of axisymmetric prolate ellipsoidal cavities, J. Mech. Phys. Solids 41 (1993) 1723–1754, https://doi.org/10.1016/0022-5096(93)90029-F.

[21] A.R. Ragab, A model for ductile fracture based on internal necking of spheroidal voids, Acta Mater. 52 (2004) 3997–4009, https://doi.org/10.1016/j.actamat.2004.05.015.

[22] S.M. Keralavarma, S. Chockalingam, A criterion for void coalescence in anisotropic ductile materials, Int J. Plast. 82 (2016) 159–176, https://doi.org/10.1016/j.ijplas.2016.03.003.

[23] O. Cazacu, B. Revil-Baudard, N. Chandola. Plasticity-Damage Couplings: From Single Crystal to Polycrystalline Materials vol. 253, Springer International Publishing, Cham, 2019, https://doi.org/10.1007/978-3-319-92922-4.

[24] S. Paik, N.N. Kumar, B.K. Dutta, P. Durgaprasad, R. Tewari, Deformation of copper single crystals: comparison of experimental results with crystal plasticity simulations, Mater. Today Commun. 24 (2020), 100997, https://doi.org/10.1016/J.MTCOMM.2020.100997.

[25] V. Tvergaard, A. Needleman, Analysis of the cup-cone fracture in a round tensile bar, Acta Metall. 32 (1984) 157–169, https://doi.org/10.1016/0001-6160(84)90213-X.

[26] B.R. Bodapati, S.P. P, P.P. Bhattacharjee, G. Sundararajan, Uniaxial compression behaviour of porous copper: experiments and modelling, Mater. Today Commun. 16 (2018) 320–329, https://doi.org/10.1016/J.MTCOMM.2018.07.008.

[27] T. Zhang, Y. Zhao, A study on the parameter identification and failure prediction of ductile metals using Gurson–Tvergaard–Needleman (GTN) model, Mater. Today Commun. 34 (2023), 105223, https://doi.org/10.1016/J.MTCOMM.2022.105223.

[28] X. Li, Z. Chen, C. Dong, Size effect on the damage evolution of a modified GTN model under high/low stress triaxiality in meso-scaled plastic deformation, Mater. Today Commun. 26 (2021), 101782, https://doi.org/10.1016/J.MTCOMM.2020.101782.

[29] M.Y. Al-Fasih, A.B.H. Kueh, S.H. Abo Sabah, M.Y. Yahya, Influence of tows waviness and anisotropy on effective Mode I fracture toughness of triaxially woven fabric composites, Eng. Fract. Mech. 182 (2017) 521–536, https://doi.org/10.1016/J.ENGFRACMECH.2017.03.051.

[30] M.Y. Al-Fasih, A.B.H. Kueh, S.H.A. Sabah, M.Y. Yahya, Tow waviness and anisotropy effects on Mode II fracture of triaxially woven composite, Steel Compos. Struct. 26 (2018) 241–253, https://doi.org/10.12989/scs.2018.26.2.241.

[31] M.Y. Al-Fasih, A.B.H. Kueh, M.H.W. Ibrahim, Failure behavior of sandwich honeycomb composite beam containing crack at the skin, PLoS One 15 (2020), e0227895, https://doi.org/10.1371/JOURNAL.PONE.0227895.

[32] H. Talebi-Ghadikolaee, H. Moslemi Naeini, E. Talebi Ghadikolaee, M.J. Mirnia, Predictive modeling of damage evolution and ductile fracture in bending process, Mater. Today Commun. 31 (2022), 103543, https://doi.org/10.1016/J.MTCOMM.2022.103543.

[33] J. Koplik, A. Needleman, Void growth and coalescence in porous plastic solids, Int J. Solids Struct. 24 (1988) 835–853, https://doi.org/10.1016/0020-7683(88)90051-0.

[34] S. Ha, K. Kim, Void growth and coalescence in f.c.c. single crystals, Int J. Mech. Sci. 52 (2010) 863–873, https://doi.org/10.1016/j.ijmecsci.2010.03.001.

[35] S.K. Yerra, C. Tekoğlu, F. Scheyvaerts, L. Delannay, P. Van Houtte, T. Pardoen, Void growth and coalescence in single crystals, Int J. Solids Struct. 47 (2010) 1016–1029, https://doi.org/10.1016/j.ijsolstr.2009.12.019.

[36] J. Zhang, S. Ding, S. Du, A damage-effect-involved phenomenological crystal plasticity model and computational methods for mechanical responses of FeCrAl alloys, Mater. Today Commun. 28 (2021), 102595, https://doi.org/10.1016/J.MTCOMM.2021.102595.

[37] C. Wu, K.W. da, Liu, Effects of void and temperature on fracture of Cu/Cu3Sn bilayers: a molecular dynamics study, Mater. Today Commun. 31 (2022), 103833, https://doi.org/10.1016/J.MTCOMM.2022.103833.

[38] A.K. Shargh, G.R. Madejski, J.L. McGrath, N. Abdolrahim, Molecular dynamics simulations of brittle to ductile transition in failure mechanism of silicon nitride nanoporous membranes, Mater. Today Commun. 25 (2020), 101657, https://doi.org/10.1016/J.MTCOMM.2020.101657.

[39] B. Liu, Z. Li, W. Li, Y. Pan, W. Wu, Molecular dynamics simulation of the porosity effect on transformation mechanism of nanocrystalline porous NiTi shape memory alloy, Mater. Today Commun. 34 (2023), 105320, https://doi.org/10.1016/J.MTCOMM.2023.105320.

[40] T.F. Guo, W.H. Wong, Void-sheet analysis on macroscopic strain localization and void coalescence, J. Mech. Phys. Solids 118 (2018) 172–203, https://doi.org/10.1016/J.JMPS.2018.05.002.

[41] M. Chouksey, S.M. Keralavarma, Ductile failure under non-proportional loading, J. Mech. Phys. Solids 164 (2022), 104882, https://doi.org/10.1016/J.JMPS.2022.104882.

[42] H.J. Guo, C. Ling, E.P. Busso, Z. Zhong, D.F. Li, Crystal plasticity based investigation of micro-void evolution under multi-axial loading conditions, Int J. Plast. 129 (2020), 102673, https://doi.org/10.1016/j.ijplas.2020.102673.

[43] C. Tekoğlu, Representative volume element calculations under constant stress triaxiality, Lode parameter, and shear ratio, Int J. Solids Struct. 51 (2014) 4544–4553, https://doi.org/10.1016/j.ijsolstr.2014.09.001.

[44] L. Morin, J.B. Leblond, A.A. Benzerga, Coalescence of voids by internal necking: Theoretical estimates and numerical results, J. Mech. Phys. Solids 75 (2015) 140–158, https://doi.org/10.1016/J.JMPS.2014.11.009.

[45] M.K. Karanam, G. Gulivindala, V.R. Chinthapenta, Effect of anisotropy on the ductile fracture in metal reinforcements of brittle matrix composites, Theor. Appl. Fract. Mech. (2021) 112, https://doi.org/10.1016/j.tafmec.2021.102923.

[46] A.A. Benzerga, J.B. Leblond, Ductile fracture by void growth to coalescence, Adv. Appl. Mech. 44 (2010) 169–305, https://doi.org/10.1016/S0065-2156(10)44003-X.

[47] G. Vadillo, J. Reboul, J. Fernández-Sáez, A modified Gurson model to account for the influence of the Lode parameter at high triaxialities, Eur. J. Mech., A/Solids 56 (2016) 31–44, https://doi.org/10.1016/j.euromechsol.2015.09.010.

[48] R.J. Asaro, Crystal plasticity, J. Appl. Mech., Trans. ASME 50 (1983) 921–934, https://doi.org/10.1115/1.3167205.

[49] Y. Huang, A user-material subroutine incorporating single crystal plasticity in the ABAQUS finite element program, Harv. Univ. Camb., MA (1991).

[50] D. Peirce, R.J. Asaro, A. Needleman, An analysis of nonuniform and localized deformation in ductile single crystals, Acta Metall. 30 (1982) 1087–1119, https://doi.org/10.1016/0001-6160(82)90005-0.

[51] Z. Chen, C. Butcher. Micromechanics modelling of ductile fracture vol. 195, Springer Dordrecht, 2013, https://doi.org/10.1007/978-94-007-6098-1.

[52] P.F. Thomason, Three-dimensional models for the plastic limit-loads at incipient failure of the intervoid matrix in ductile porous solids, Acta Metall. 33 (1985) 1079–1085, https://doi.org/10.1016/0001-6160(85)90201-9.

[53] J.C. Zhu, M. ben Bettaieb, F. Abed-Meraim, Investigation of the competition between void coalescence and macroscopic strain localization using the periodic homogenization multiscale scheme, J. Mech. Phys. Solids 143 (2020), 104042, https://doi.org/10.1016/J.JMPS.2020.104042.

[54] X. Gao, J. Kim, Modeling of ductile fracture: significance of void coalescence, Int J. Solids Struct. 43 (2006) 6277–6293, https://doi.org/10.1016/j.ijsolstr.2005.08.008.

[55] H.J. Guo, D.F. Li, Crystal plasticity-based micromechanical finite element modelling of ductile void growth for an aluminium alloy under multiaxial loading conditions, Proc. Inst. Mech. Eng., Part L: J. Mater.: Des. Appl. 233 (2019) 52–62, https://doi.org/10.1177/1464420718805828.

[56] V. Vishwakarma, S.M. Keralavarma, Micromechanical modeling and simulation of the loading path dependence of ductile failure by void growth to coalescence, Int J. Solids Struct. 166 (2019) 135–153, https://doi.org/10.1016/j.ijsolstr.2019.02.015.

[57] B. Budiansky, J.W. Hutchinson, S. Slutsky, Void growth and collapse in viscous solids, Mech. Solids 0 (1982) 13–45, https://doi.org/10.1016/b978-0-08-025443-2.50009-4.

[58] M.K. Karanam, V.R. Chinthapenta, Void growth and morphology evolution during ductile failure in an FCC single crystal, Contin. Mech. Thermodyn. 33 (2021) 497–513, https://doi.org/10.1007/s00161-020-00922-z.